Chapter 7

Solar Water Heater and TEG-based Hybrid System with Fishtail Vortex Generators

Overview: This chapter examines the performance of a hybrid system that combines an Evacuated U-tube Solar Water Heater (EUSWH) with a Thermoelectric Generator (TEG). To improve thermal and electrical efficiency, fishtail vortex generators (FVGs) are positioned on the hot side of the TEG module. The study explores how key operating factors, such as incident solar radiation intensity, water mass flow rate, inlet EUSWH temperature, and the presence of vortex generators, affect the performance of the EUSWH, TEG, and the overall system. The hybrid setup simultaneously provides heated water and electrical power, with vortex generators playing a crucial role in enhancing its overall effectiveness.

7.1 System description

Fig. 7.1 depicts the proposed EUSWH-TEG hybrid system. The hybrid system comprises an Evacuated U-tube Solar Water Heater (EUSWH), a Thermoelectric Generator (TEG), and the cold and hot channels. The cold water first enters the cold side of the TEG through the cold side channel. After this, the cold water goes into the solar water heater. The solar radiation falling onto the EUSWH heats the water, raising its temperature. This hot water then flows through the hot water channel after which it can be used for various purposes. The TEG is sandwiched between the cold and the hot channel. The temperature difference across the TEG results in an electric potential difference across its legs due to the Seebeck effect. Thus, electrical energy is also produced along with the hot water. Q_{SUN} denotes the solar radiation received by the EUSWH in W. The ambient temperature is denoted by T_0. $T_{in,EUSWH}$, and $T_{out,EUSWH}$ denote the bulk temperature of water entering and leaving the EUSWH, respectively. $T_{in,cold}$, $T_{out,cold}$, $T_{in,hot}$, and $T_{out,hot}$ represent the bulk temperatures of water at the inlet of the cold channel, outlet of the cold channel, inlet of the hot channel, and outlet of the cold channel, respectively.

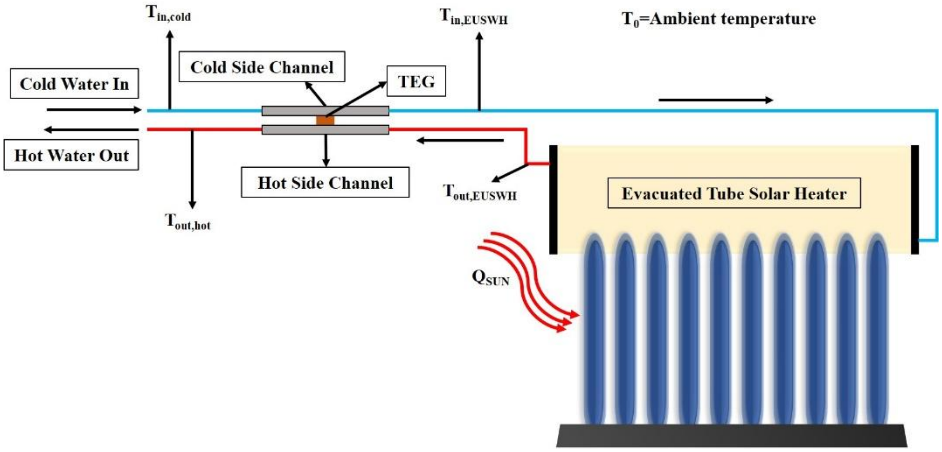

Fig. 7.1 EUSWH-TEG hybrid system schematic diagram

7.1.1 Evacuated U-tube solar water heater

The section view of a single U-tube is shown in Fig. 7.2. On the outside, the EUSWH embraces vacuum U-tubes in tandem and a tank for hot water storage.

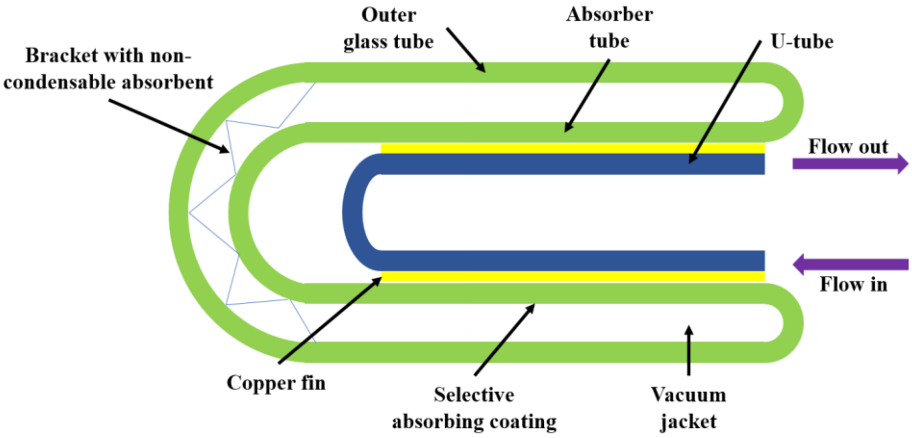

Fig. 7.2 Section view of a single U-tube of EUSWH

The U-tube contains a two-layer structure made of coated-vacuum glass tubes. The absorber tube is equipped with a selective coating on its surface, while the vacuum jacket minimizes conduction losses. Circular copper fins are used to attach or weld the tubes, facilitating the transport of solar energy captured by specialized absorptive coating to water flowing through the U-tube. The parameter values utilized in the EUSWH system are presented in Table 7.1. The EUSWH model has been developed using the Engineering Equation Solver code. To ensure a thorough analysis and simplify complex calculations without compromising accuracy, the following assumptions are made for the EUSWH system (Zhang et al., 2024):

- Heat transfer is considered one-dimensional and steady-state, with transient effects excluded.
- The heat resistance of the outer glass tube and its capacity to absorb solar irradiation are neglected.
- The working fluid's velocity within the tube is assumed to remain constant.
- The phase of the working fluid does not change.
- Heat losses within the vacuum layer are disregarded.

Table 7.1: Parameters used for the EUSWH

Parameter	Symbol	Value
Inner absorber tube’s outer diameter	d_{SC}	0.047m
Inner absorber tube’s effective length	L_{SC}	1.71m
Cross sectional area of the tube	A_t	1 x 10^{-3}m^2
Absorbing coating’s absorptivity	α_a	0.9
Outer glass’s light transmittance	τ	0.9
Number of tubes	N	36

Collector efficiency factor	F'	0.9
Ambient temperature	T_0	298K
Heat transfer coefficient at the fluid-tube wall interface	$h_{f,i}$	700W/m^{2}K

The EUSWH utilizes the solar irradiance falling onto it to heat the water which can be used for further purposes. The part of the solar energy absorbed by the EUSWH is called the useful solar energy Q_{EUSWH}. The Q_{EUSWH} is the difference between total incident solar energy and the heat lost to the environment (Q_E) and is given as follows:

$$Q_{EUSWH} = Q_{SUN} - Q_E = F_R\left[G \cdot \tau \cdot \alpha_a \cdot A_e - A_a \cdot U_L\left(T_{in,EUSWH} - T_0\right)\right] \tag{7.1}$$

Where F_R is the EUSWH's heat removal factor, G is the solar radiation, τ is the outer glass's light transmission, α is the selective coating's absorptivity, and U_L is the EUSWH's total heat loss coefficient. The areas A_e represents the effective heat absorption area of the absorber and A_a represents the outer surface area of the absorber (Zhang et al., 2024), and have been calculated as below:

$$A_e = N(1.43 d_{SC} \cdot L_{SC}) \tag{7.2}$$

$$A_a = N(\pi \cdot d_{SC} \cdot L_{SC}) \tag{7.3}$$

Where, d_{SC} and L_{SC} represent the outer diameter of the inner absorber tube, and the effective length of the inner absorber tube, respectively. The EUSWH's total heat loss coefficient, U_L (Zhang et al., 2024), has been determined as follows:

$$U_L = 0.003(T_i - T_0) + 0.89 \tag{7.4}$$

The EUSWH's heat removal factor is a function of the mass flow rate ($\dot{m}_w$) and heat capacity of water ($C_{p,w}$), the outer surface area of absorber tubes, EUSWH's heat loss coefficient, and the efficiency factor of the EUSWH (F'). It is calculated as follows:

$$F_R = \frac{\dot{m}_w \cdot C_{p,w}}{A_a \cdot U_L}\left[1 - \exp\left(-\frac{A_a \cdot U_L \cdot F}{\dot{m} \cdot C_{p,w}}\right)\right] \tag{7.5}$$

Where,

$$F' = \frac{\frac{1}{U_L}}{W\left[\frac{1 + \frac{U_L}{C_b}}{U_L[d + (W - d)F]} + \frac{1}{C_B} + \frac{1}{h_{f,i}}\right]} \tag{7.6}$$

$$\dot{m}_w = u_w \cdot \rho_w \cdot A_t \tag{7.7}$$

In the above equations, C_b, C_B, W, d, F, u_w, ρ_w, and A_t denote the integrated conductance, bond conductance, distance around the U-tubes, diameter of the U-tube, and efficiency standard for straight fins, flow velocity of water in tubes, density of water, and U-tube's cross-sectional area respectively. Furthermore, the useful solar energy and the bulk temperature of the water leaving the EUSWH can be calculated as follows:

$$Q_{EUSWH} = \dot{m}_w \cdot C_{p,w}\left(T_{out,EUSWH} - T_{in,EUSWH}\right) \tag{7.8}$$

$$T_{out,EUSWH} = T_{in,EUSWH} + \frac{F_R}{C_{p,w} \cdot u_w}\left[G \cdot \tau \cdot \alpha_a \cdot A_e - A_a \cdot U_L\left(T_{in,EUSWH} - T_0\right)\right] \tag{7.9}$$

Thus, with all the above parameters calculated, we can find the efficiency of the EUSWH which is defined as follows:

$$\eta_{EUSWH} = \frac{Q_{EUSWH}}{G \cdot A_e} \tag{7.10}$$

7.1.2 Thermoelectric Generator

A TEG comprises ceramic plates, solder, load resistance (R_L), and multiple sets of positive and negative thermoelectric legs (Fig. 7.3). The legs are connected electrically in series and thermally in parallel. Except at the junctions and ceramic plate and the channels, the TEG is electrically and thermally insulated elsewhere. As hot water flows through the hot water channel, it heats the ceramic plate of the TEG. The temperature difference across the thermoelectric elements causes electricity generation due to the Seebeck effect. To enhance research efficiency, streamline intricate calculations, and ensure accuracy, the TEG system is based on the following assumptions (Shen et al., 2016):

- The EUSWH and TEG operate in steady states.
- The Thomson effect in thermoelectric elements of the TEG is neglected, and electric current is assumed to flow past the device's arm uninterrupted.
- The average Seebeck coefficient of the TEG is treated as constant at a uniform temperature.

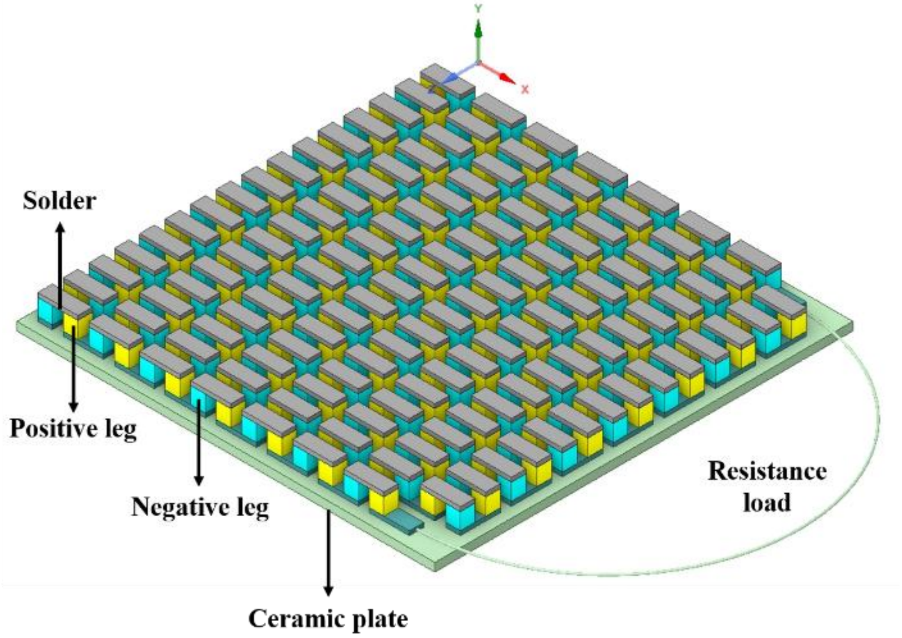

Fig. 7.3 TEG with its components

The properties of the commercially available Bi_2Te_3 and the TEG leg geometry description are given in Table 7.2 where l_{TEG}, b_{TEG}, and h_{TEG} denote the length, breadth, and height of the TEG leg, respectively. Bi_2Te_3 is a widely used thermoelectric material recognized for its advanced development and excellent reliability. Its suitable temperature range corresponds closely to the operating range of the EUSWH, making it a preferred option for the thermoelectric elements. The choice of material for the ceramic plates and the solder are aluminum oxide and copper respectively. The channels and the TEG have been numerically simulated on ANSYS 2022R2.

Table 7.2: Thermoelectric properties of Bi_2Te_3 and leg dimensions (Zhang et al., 2024)

Property	Expression
Seebeck coefficient (V/K)	$\alpha_p(T) = 5.921376 \times 10^{-13}T^3 - 3.274207 \times 10^{-9}T^2 + 2.422355 \times 10^{-6}T - 2.743842 \times 10^{-4}$ $\alpha_n(T) = 1.291689 \times 10^{-13}T^3 + 1.074408 \times 10^{-9}T^2 - 9.271759 \times 10^{-7}T + 8.958888 \times 10^{-6}$
Electrical conductivity (S/m)	$\sigma_p(T) = [2.248899 \times 10^{-14}T^3 - 1.250867 \times 10^{-10}T^2 + 1.388189 \times 10^{-7}T - 2.244786 \times 10^{-5}]^{-1}$ $\sigma_n(T) = [-1.24614 \times 10^{-14}T^3 - 6.429015 \times 10^{-11}T^2 + 9.103036 \times 10^{-8}T - 1.049646 \times 10^{-5}]^{-1}$
Thermal conductivity (W/m^2K)	$k_p(T) = 1.251606 \times 10^{-7}T^3 - 1.242845 \times 10^{-4}T^2 + 3.873788 \times 10^{-2}T - 2.362707$ $k_n(T) = -1.592653 \times 10^{-8}T^3 + 2.905845 \times 10^{-5}T^2 - 1.58323 \times 10^{-2}T + 3.727526$
$l_{TEG} = b_{TEG}$	1.4mm
h_{TEG}	1.6mm

Based on the above assumptions and parameters, the heat transfer on the hot side ($Q_{h,TEG}$), heat transfer on the cold side ($Q_{c,TEG}$), the power generated ($Power_{TEG}$), and the TEG efficiency (η_{TEG}) are given as follows:

$$Q_{h,TEG} = N\left[\alpha_{pn} I T_{h,TEG} + k_{pn}\left(T_{h,TEG} - T_{c,TEG}\right) - \frac{I^2 R_{pn}}{2}\right] \tag{7.11}$$

$$Q_{c,TEG} = N\left[\alpha_{pn} I T_{c,TEG} + k_{pn}\left(T_{h,TEG} - T_{c,TEG}\right) + \frac{I^2 R_{pn}}{2}\right] \tag{7.12}$$

$$Power_{TEG} = Q_{h,TEG} - Q_{c,TEG} = \alpha_{pn} I\left(T_{h,TEG} - T_{c,TEG}\right) - R_{pn} I^2 \tag{7.13}$$

$$\eta_{TEG} = \frac{Power_{TEG}}{Q_{h,TEG}} = \frac{\alpha_{pn} I\left(T_{h,TEG} - T_{c,TEG}\right) - R_{pn} I^2}{N\left[\alpha_{pn} I T_{h,TEG} + k_{pn}\left(T_{h,TEG} - T_{c,TEG}\right) - \frac{I^2 R_{pn}}{2}\right]} \tag{7.14}$$

7.1.3 Water flow channels

Fig. 7.4 shows the part of the hybrid system where thermoelectric generation comes into play. For the thermoelectric generator analysis, two configurations on the hot side of the TEG have been considered, viz. smooth channel and channel equipped with fishtail vortex generators (FVGs). The length, breadth, and height of the channel are 360mm x 70mm x 20mm, respectively. The channel and the VG material have been selected as aluminum due to its high thermal conductivity. The definition of the angle of inclination, the fishtail VG configuration, and the schematic of flow past the VG are shown in Fig. 7.5 (a-c). The thickness of the VG is 1mm while the angle of inclination selected is 60° as per the previous study.

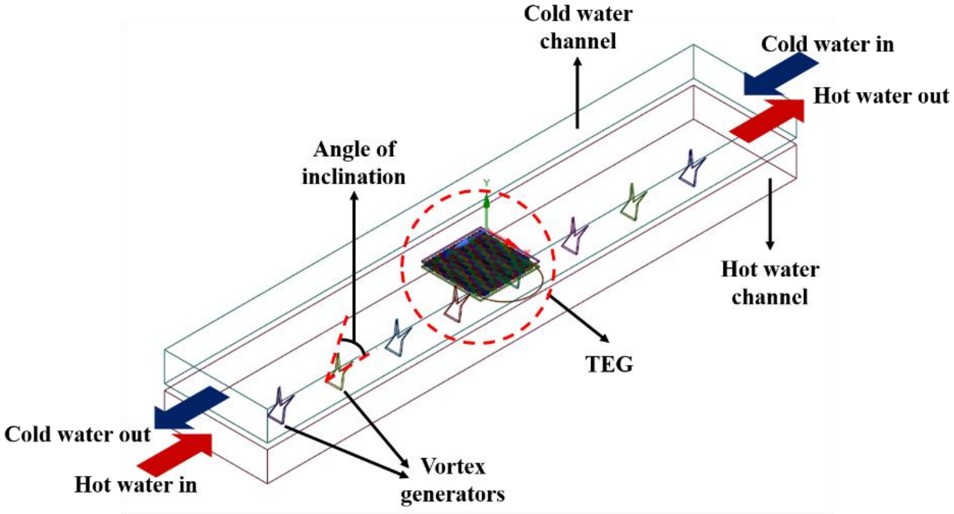

Fig. 7.4 TEG sandwiched between cold channel and hot channel (equipped with FVGs)

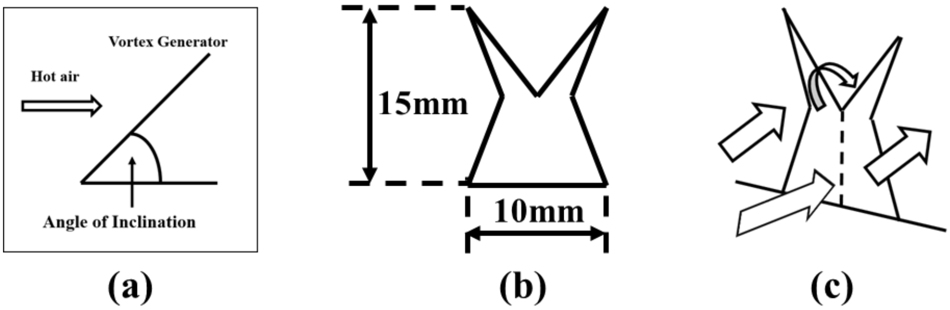

Fig. 7.5 (a) Angle of inclination, (b) FVG dimensions, and (c) FlowPast FVG

In this study, the considered hot air is treated as incompressible and continuous, and the simulations are conducted under stable states. The determination of the heat exchanger surface temperature is achieved through the application of conjugate heat transfer Eqs. within the computational unit. The governing Eqs. are as follows:

Continuity Eq., $\frac{\partial}{\partial x_i}(\rho u_i) = 0$ (7.15)

Momentum Eq., $\frac{\partial}{\partial x_i}(\rho u_i u_k) = \frac{\partial}{\partial x_i}\left(\mu \frac{\partial u_k}{\partial x_i}\right) - \frac{\partial p}{\partial x_k}$ (7.16)

Energy Eq., $\frac{\partial}{\partial x_i}(\rho u_i T) = \frac{\partial}{\partial x_i}\left(\Gamma \frac{\partial T}{\partial x_i}\right)$ (7.17)

Here, ρ and μ represent density and dynamic viscosity, respectively. The diffusion coefficient Γ is defined as thermal conductivity divided by the specific heat ($\Gamma = k/Cp$). Eqs. (7.18) and (7.19) simulate turbulent flow using k-ε model.

$$\frac{\partial}{\partial x_i}(\rho k u_i) = \frac{\partial}{\partial x_j}\left[\left(\mu + \frac{\mu_t}{\sigma_k}\right)\frac{\partial k}{\partial x_j}\right] + G_k + G_b - \rho\epsilon - Y_M + S_k \tag{7.18}$$

$$\frac{\partial}{\partial x_i}(\rho \epsilon u_i) = \frac{\partial}{\partial x_j}\left[\left(\mu + \frac{\mu_t}{\sigma_\epsilon}\right)\frac{\partial \epsilon}{\partial x_j}\right] + C_{1\epsilon}\frac{\epsilon}{k}(G_k + C_{3\epsilon}G_b) - C_{2\epsilon}\rho\frac{\epsilon^2}{k} + S_\epsilon \tag{7.19}$$

Within this framework, G_k, G_b, and Y_M signify the creation of turbulence kinetic energy arising from the mean velocity gradient, buoyancy effects, and the involvement of fluctuating dilation in turbulence towards the comprehensive dissipation rate. The constants $C_{1\epsilon}$, $C_{2\epsilon}$, and $C_{3\epsilon}$ play a crucial role in these formulations. The turbulent viscosity, μ_t, is modeled as:

$$\mu_t = \rho C_\mu \frac{k^2}{\epsilon} \tag{7.20}$$

The production of k is defined by the following Eqs:

$$P_k = -\rho \overline{u_i' u_j'} \frac{\partial u_j}{\partial x_i} \tag{7.21}$$

$$P_k = \mu_t S^2 \tag{7.22}$$

Where the mean rate of strain tensor, S, is:

$$S \equiv \sqrt{2S_{ij}S_{ij}} \tag{7.23}$$

7.1.4 Hybrid system

The overall hybrid system performance can be evaluated by ascertaining the hybrid system efficiency (η_{HS}). The TEG is responsible for the electrical power generation in the hybrid system, while the input to the hybrid system is free solar energy. Hence, the hybrid system efficiency is defined as (Zhang et al., 2024):

$$\eta_{HS} = \frac{Power_{TEG}}{Q_{SUN}} = \frac{\alpha_{pn} I \left(T_{h,TEG} - T_{c,TEG}\right) - R_{pn} I^2}{G.A_e} \tag{7.24}$$

7.1.5 Validation and Grid Independence Test

The coupling of the EUSWH-TEG hybrid system has not been done experimentally before, thus the validation for the EUSWH-TEG hybrid system is provided in the current work. So, the model validation of EUSWH and TEG has been validated with experimental results. If the models of the EUSWH and TEG are reliable, then it can ensure that the present EUSWH-TEG hybrid system model has achieved a satisfactory level. In Fig. 7.6 (a) the variation of η_{EUSWH} with $(T_{in,EUSWH}-T_0)/G$ is represented, while the voltage changes with the temperature difference have been illustrated in Fig. 7. 6 (b).

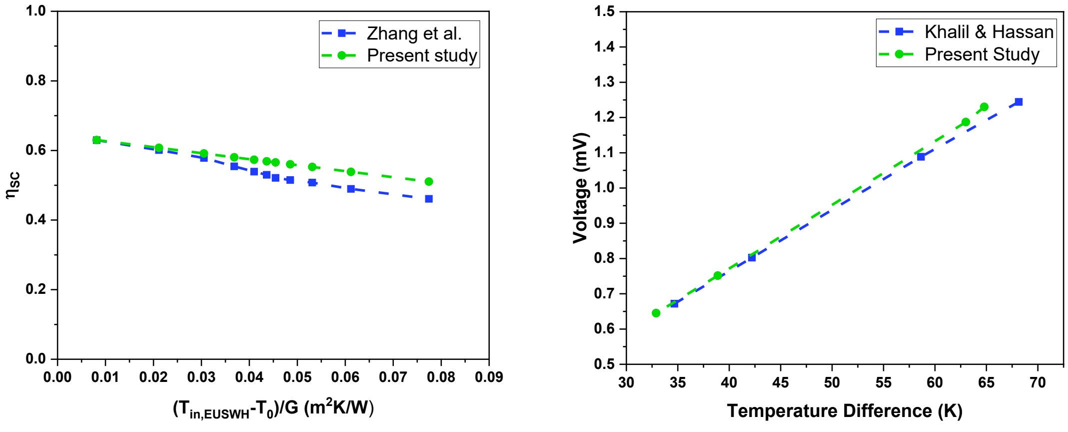

(a) **(b)**

Fig. 7.6 (a) Validation of present EUSWH with experimental results (b) Comparison of present numerical data and experimental work

In Fig. 7.6 (a), it is observed that the numerical model curve runs near the experimental study curve (Zhang et al., 2024). Furthermore, the maximum relative error calculated is 8.76%, suggesting the reliability of the EUSWH model. Also, Fig. 7.6 (b) represents the validation of the numerical model of TEG of the present study with that of an experimental one (Khalil and Hassan, 2020). The maximum discrepancy observed is 3.44%, depicting the high consistency of the current model. The limited deviation obtained in both validations might be the result of the assumption made before. The advantage of the study is, however, that it has been conducted within the same range as the validation, hence, the deviation will not exceed the maximum error value obtained.

The detailed simulations performed for the 3D TEG system require precise mesh generation to accurately evaluate the distributions of thermohydraulic and thermoelectric parameters. Various mesh sizes are applied to different regions within each computational domain to account for the complexities of VGs and TEG components. Due to the intricate structure of VGs, a fine quad mesh is adopted for the fluid and plate regions, while an even finer quad mesh is used for the TEG domain, given its compact size and numerous contact points, as illustrated in Fig. 7.7.

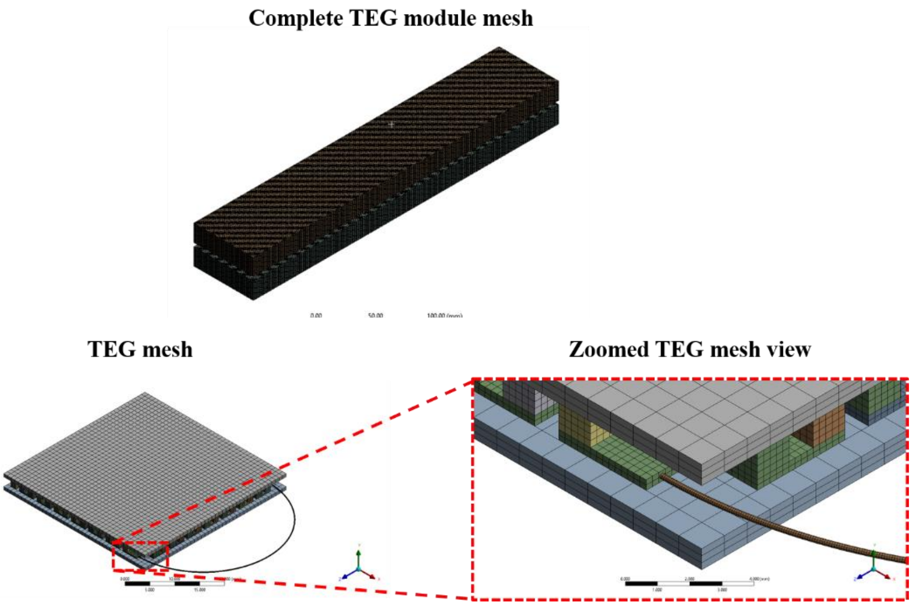

Fig. 7.7 TEG module meshing

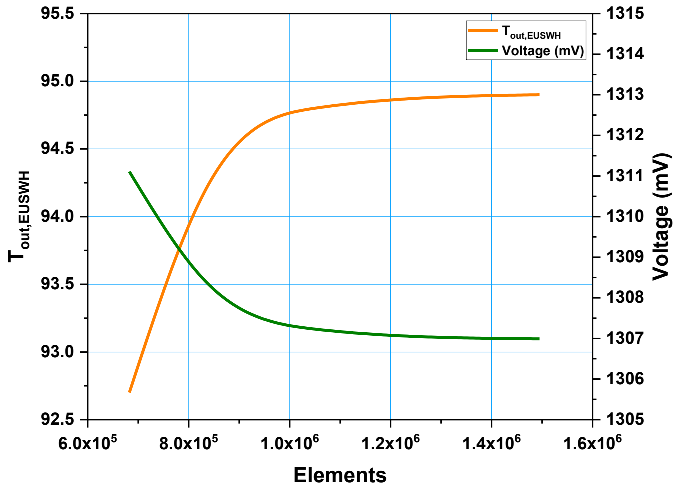

Fig. 7.8 Grid independency test

Four distinct grid configurations, ranging from 682,424 to 1,494,990 elements, were analyzed. Fig. 7.8 demonstrates that the grid configuration comprising 1,049,230 cells exhibits a relative variation of less than 1% in the outlet EUSWH temperature and TEG voltage compared to the configuration with the highest cell count (1,494,990). Consequently, for subsequent simulations, the grid configuration with 1,049,230 cells, or a closely similar setup, was chosen as the standard grid size, balancing computational efficiency and processing time.

7.2 Results and Discussion

The novel EUSWH-TEG hybrid system with the application of vortex generators in the system has been developed in the present study. This section comprises the analysis of performance metrics of the EUSWH, the TEG, and the EUSWH-TEG hybrid system. The performance metrics of the EUSWH studied include EUSWH's outlet temperature, useful solar energy, and EUSWH efficiency. Additionally, the TEG output parameters such as voltage, current, power, and TEG efficiency have been analyzed which also incorporates the impact of fishtail vortex generators (FVGs) employed in the hot water channel. Eventually, to scrutinize the hybrid system, its efficiency is evaluated. The study incorporates multi-dimensional input parameters for the comprehensive study of the hybrid system.

7.2.1 EUSWH performance

The EUSWH performance has been studied for the incident solar radiation (100-1000W/m^2), the mass flow rate of water (0.01-0.02kg/s), and EUSWH inlet temperature (303-313K). From Fig. 7.9 (a-c) it is observed that $T_{out,EUSWH}$ increases as the solar radiation and $T_{in,EUSWH}$ is raised. However, $T_{out,EUSWH}$ decreases as the mass flow rate input to the EUSWH is increased. The decrease in $T_{out,EUSWH}$ is more pronounced at higher values of solar radiation and low mass flow rate. It is also directly influenced by $T_{in,EUSWH}$. The reason behind this is simple to understand. Higher solar radiation means more energy is available for heating the water. Solar radiation is the primary source of energy in the system. When solar radiation increases, the collector absorbs more energy, raising the temperature of the working fluid (water). The useful solar heat (Q_{EUSWH}) from the sun (Q_{SUN}) increases with solar radiation, leading to a higher outlet temperature (Kumar et al., 2021). The explanation is also supported by Eq. 7.8. A lower mass flow rate allows the water more time to absorb heat, increasing the outlet temperature. When the flow rate is reduced, the residence time of water in the collector increases. This longer duration allows the water to absorb more heat per unit mass. This is in good agreement with Eq. 7.8. A critical point to note here is that $T_{in,EUSWH}$ has a positive impact on $T_{out,EUSWH}$ than the mass flow rate at a particular incident solar radiation. For instance, at G=1000W/m^2, $T_{out,EUSWH}$ increases by 2.45% and 2.85% at mass flow rates of 0.01 and 0.02kg/s, respectively when the $T_{in,EUSWH}$ varies from 303-313K. However, it decreases by 4.57% and 4.2% at $T_{in,EUSWH}$ of 303 and 313K, respectively when mass flow rates are varied from 0.01-0.02kg/s.

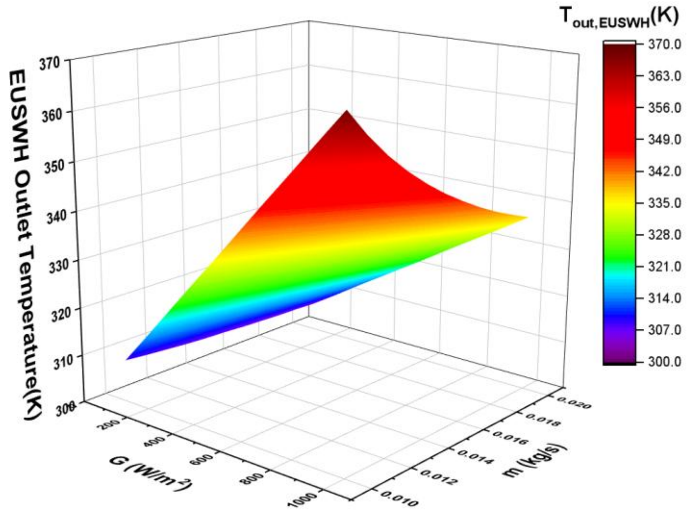

(a)

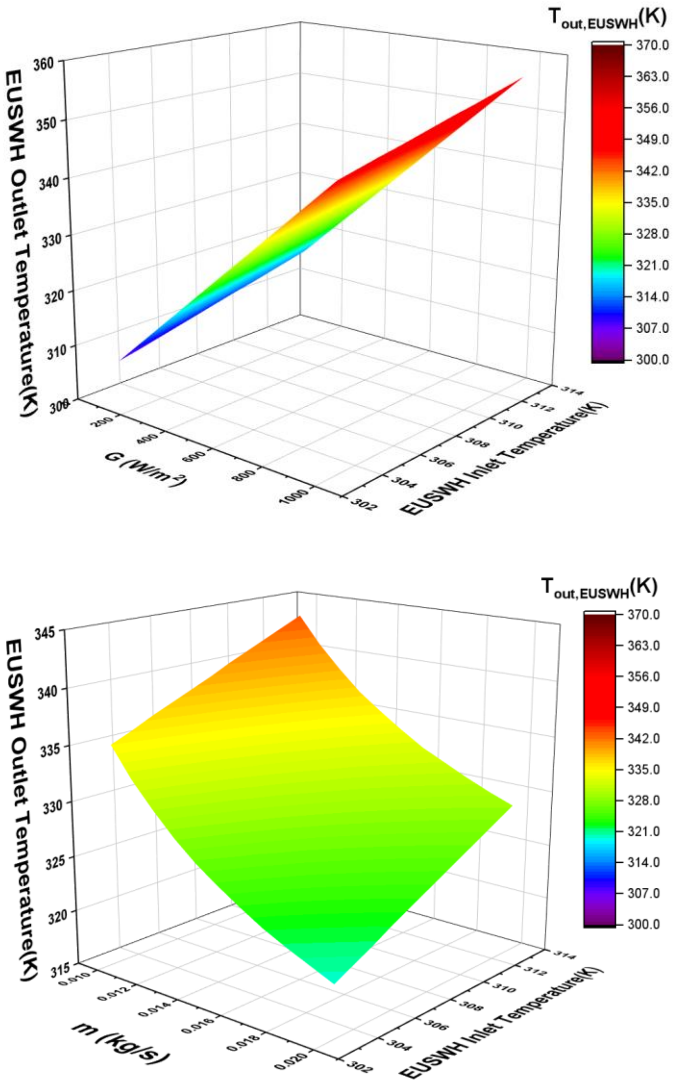

(b)

(c)

Fig. 7.9 (a-c) Effect of incident solar radiation, mass flow rate, and inlet EUSWH temperature on the outlet EUSWH temperature

The impact of incident solar radiation, water mass flow rate, and EUSWH inlet temperature on the useful solar energy or the solar energy absorbed by it can be seen in Fig. 7.10 (a-c). It is observed that Q_{EUSWH} increases with G. It is obvious that more incident radiation will upsurge the amount of solar energy being absorbed by the EUSWH. With the increase in the mass flow rate of water, a marginal increment in Q_{EUSWH} is observed. Q_{EUSWH} increases to some extent at high values of incident solar radiation, while at lower values of G, the increment is negligible, as the mass flow rate is varied. With the increase in $T_{in,EUSWH}$, the useful solar energy is decreased. This is because heat transfer is a strong function of temperature difference. As inlet EUSWH temperature is increased, the heat transfer rate decreases due to decreased temperature difference. The highest achievable heat absorption rate is 1408 W at G=1000W/m^2, mass flow rate=0.02kg/s, and inlet EUSWH temperature=303K. At G=1000W/m^2, at the mass flow rate of 0.01kg/s, the Q_{EUSWH} decreases by 5.56%, while at 0.02kg/s, the decrement is 5.4% when $T_{in,EUSWH}$ is varied between 303 to 313K. However, at 303K and 313K, Q_{EUSWH} increases by 4.45% and 4.63%, respectively when the flow rate is varied from 0.01-0.02kg/s.

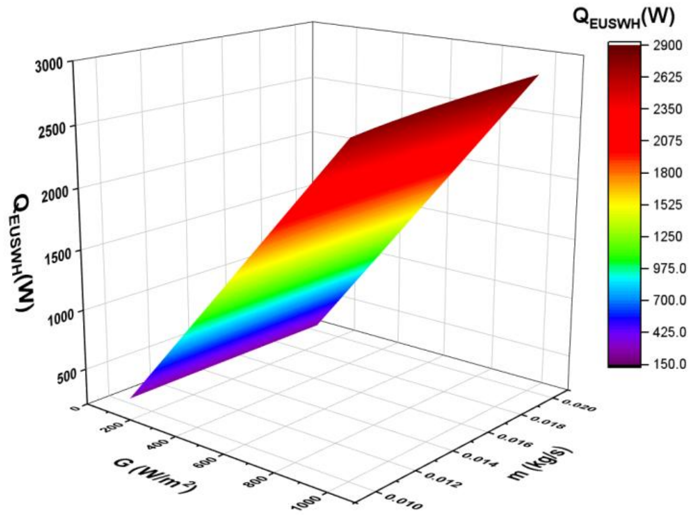

(a)

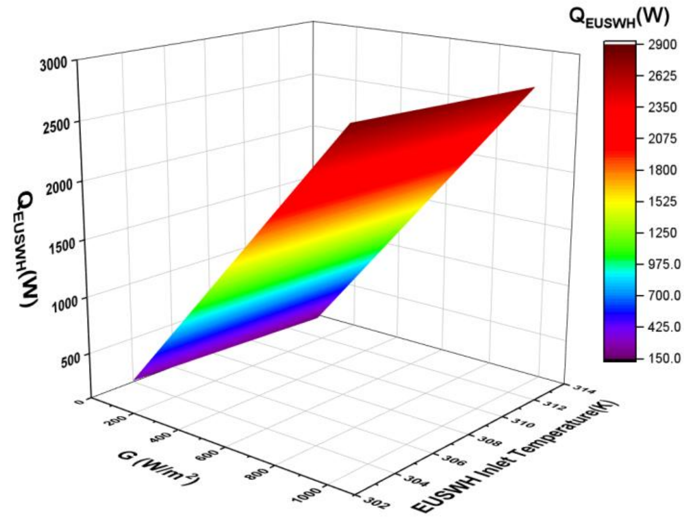

(b)

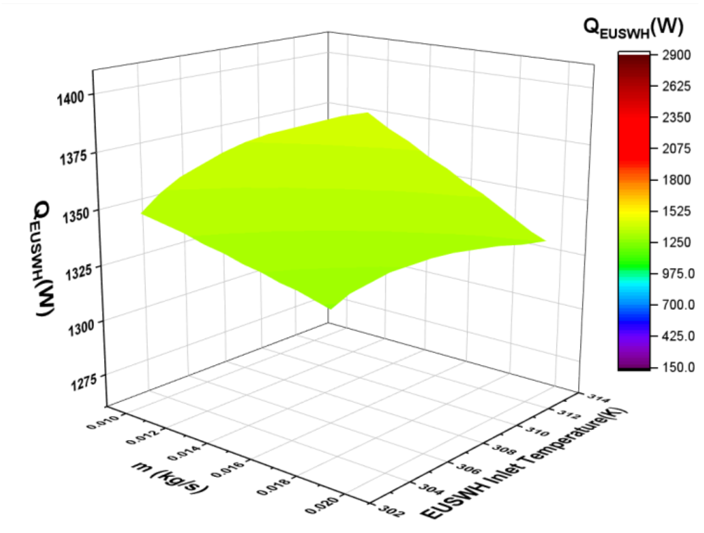

(c)

Fig. 7.10 (a-c) Effect of incident solar radiation, mass flow rate, and inlet EUSWH temperature on the useful solar energy

Fig. 7.11 (a-c) depicts the EUSWH efficiency variation with the incident solar radiation, water mass flow rate, and EUSWH inlet temperature. It can be easily observed that η_{EUSWH} increases with an increase in incident solar radiation, and mass flow rate, while it decreases with inlet EUSWH temperature. The solar radiation incident on the absorber tube directly supplies the energy for heating the water. When the incident solar radiation increases, the absorber tube absorbs more energy, leading to a higher temperature gradient between the tube and the water inside. This increases the rate of heat transfer to the water. Moreover, higher mass flow rates mean lower water outlet temperatures for a given incident energy, reducing thermal losses from the system to the surroundings. Hence the η_{EUSWH} increases with mass flow rate. When $T_{in,EUSWH}$ increases, the absorber loses more heat to the surroundings (thermal losses increase) because of the higher temperature difference between the absorber and the ambient air. The system's ability to extract energy from solar radiation diminishes, lowering its thermal efficiency. Another critical point to note here is that $T_{in,EUSWH}$ has a greater impact on η_{EUSWH} than the mass flow rate at a particular incident solar radiation. For instance, at G=1000W/m^2, η_{EUSWH} decreases by 5.55% and 4.92% at mass flow rates of 0.01 and 0.02kg/s, respectively when the $T_{in,EUSWH}$ varies from 303-313K. However, it increases by 3.88% and 4.58% at $T_{in,EUSWH}$ of 303 and 313K, respectively when mass flow rates are varied from 0.01-0.02kg/s. Furthermore, the increment in η_{EUSWH} gradually decreases as G increases due to increased losses at higher solar radiation. Also, at low G, $T_{in,EUSWH}$ has a great influence on η_{EUSWH}.

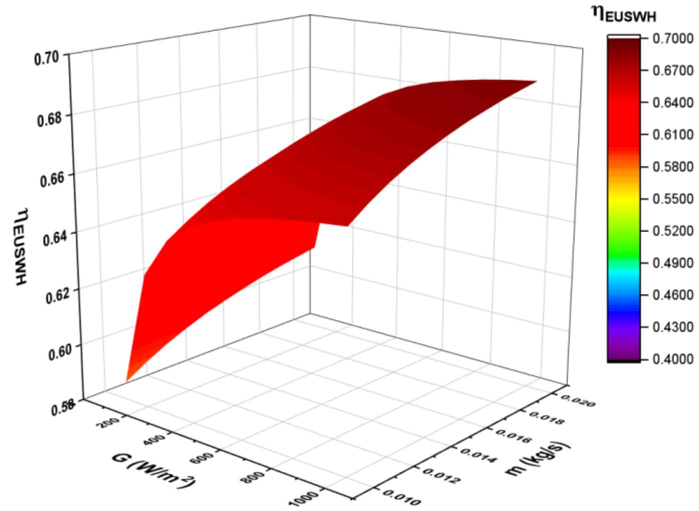

(a)

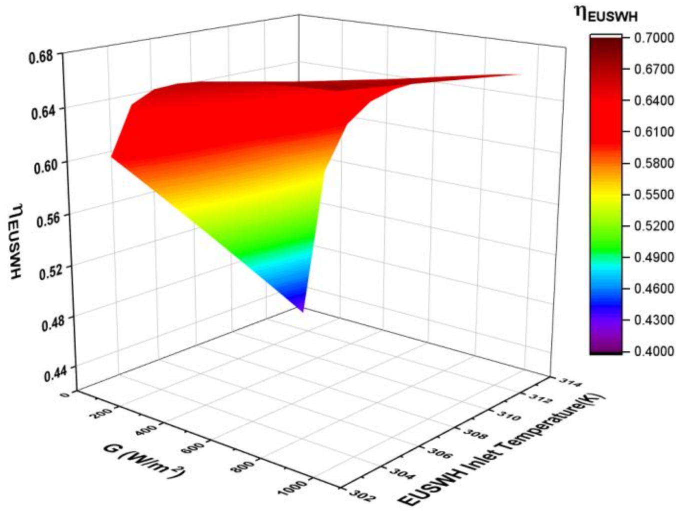

(b)

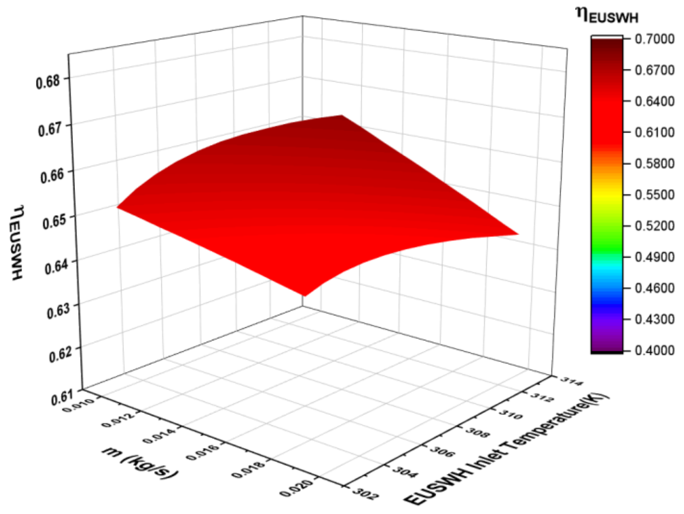

(c)

Fig. 7.11 (a-c) Effect of incident solar radiation, mass flow rate, and inlet EUSWH temperature on η_{EUSWH}

From the above analysis, it is observed that peak EUSWH performance is attained at the highest *G*. However, as the mass flow rate increases $T_{out,EUSWH}$ decreases while Q_{EUSWH} and η_{EUSWH} increase. The inlet EUSWH temperature shows the opposite trend and $T_{out,EUSWH}$ increases, Q_{EUSWH} and η_{EUSWH} decreases. So, it becomes important to study the further system at the minimum and maximum mass flow rates (0.01 and 0.02kg/s) and $T_{in,EUSWH}$ (303 and 313K) at the maximum incident solar radiation (1000W/m^2) to effectively investigate the TEG and hybrid system performance independently.

7.2.2 TEG performance

TEG performance parameters like voltage, current, power, and efficiency have been studied in this section inclusive of the fishtail vortex generator (FVG) impact on the TEG outputs. The performance of TEG for smooth and VG-employed channels for different mass flow rates at $T_{in,EUSWH}$ of 303K is shown in Fig. 7.12 (a-b). The application of VGs results in better TEG performance. The objective of employing VGs is achieved as they result in enhanced heat transfer and uniform temperature along the channel.

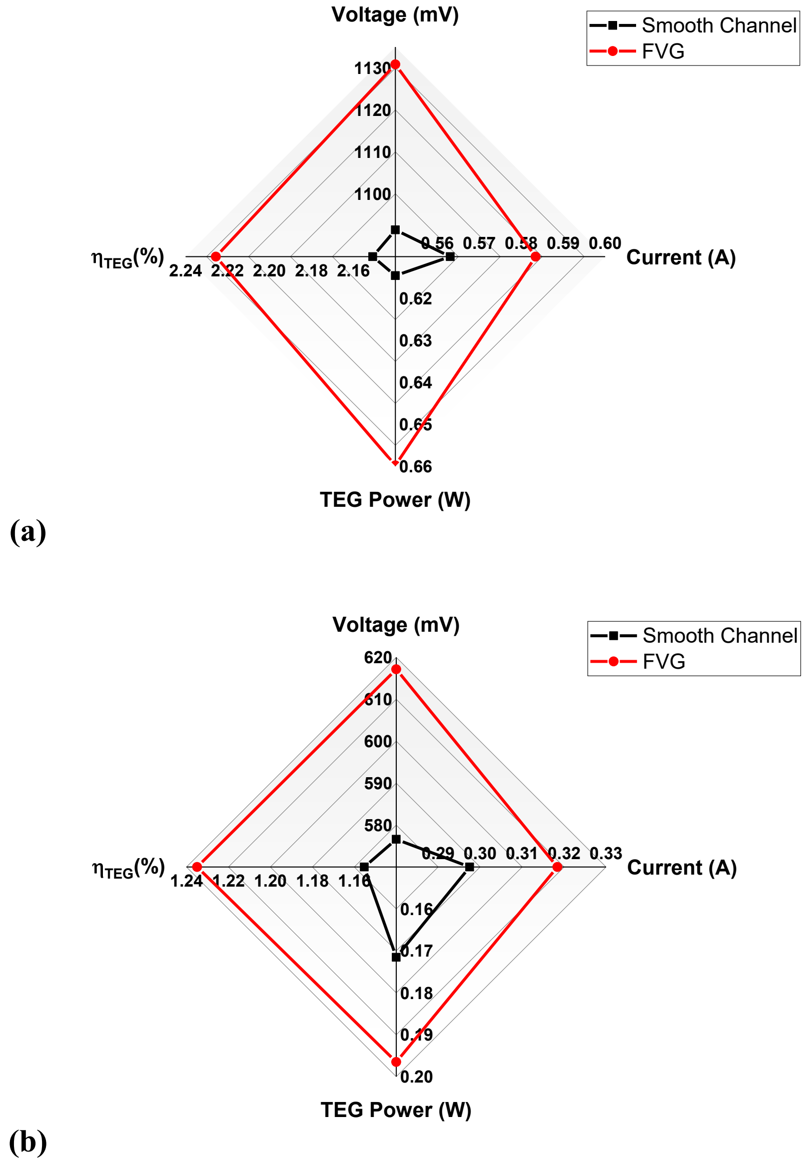

Fig. 7.12 TEG performance parameter at 303K, at (a) 0.01kg/s, and (b) 0.02kg/s

The mixing caused by vortices disrupts the laminar boundary layer and enhances convective heat transfer. This ensures that thermal energy is transported more efficiently from the working fluid to the channel walls and subsequently to the TEG modules. Furthermore, vortex generators disturb the thermal boundary layer, thinning it and making it more receptive to heat transfer. The continuous disruption ensures higher local heat transfer coefficients. Also, the generated vortices transition the flow towards turbulence or enhance the local turbulence intensity, which increases the convective heat transfer rate. For a mass flow rate of 0.01kg/s the voltage, current, power, and TEG efficiency increase by 3.62%, 3.61%, 7.36%, and 3.47% respectively, when VGs are put to use. While at 0.02kg/s, the same parameters increased by 7.03%, 7.02%, 14.56%, and 5.13%. A similar trend can be seen in Fig. 7.13 (a-b). The vortex generator helps in achieving higher outputs. The vortex generators are simple structure and their presence negligibly increases the weight of the TEG module. FVGs introduce secondary flows in the form of streamwise and transverse vortices, which improve the mixing of hot and cold fluid layers. They minimize flow stagnation zones, where heat transfer would otherwise be less effective due to low fluid velocity. The improved heat transfer raises the temperature gradient across the TEG modules, directly increasing the output voltage and current. A higher thermal gradient translates into greater electrical power generation, enhancing the TEG's overall output. Efficient heat extraction and better utilization of thermal energy result in higher thermal-to-electric conversion efficiency. They provide additional benefits by reducing hot spots, and compact system design. The uniformity in heat transfer prevents localized overheating, improving the durability and performance consistency of the TEG. The higher heat transfer rates achieved with vortex generators allow for more compact system designs, reducing material costs and system weight. For a mass flow rate of 0.01kg/s and 313K; the voltage, current, power, and TEG efficiency increase by 3.73%, 3.72%, 7.61%, and 3.58% respectively, when VGs are used. While at 0.02kg/s, the same parameters increased by 7.26%, 7.16%, 15.04%, and 7.12%. Further analysis shows that the vortex generators are more efficient at lower $T_{in,EUSWH}$ in terms of the absolute values of the performance parameters. For instance, the TEG efficiency for channels with FVGs at 303 and 313K are 2.66% and 2.55% respectively. However, in terms of relative performance, higher sensitivity is observed in higher $T_{in,EUSWH}$. The result is consistent with Zhang et al. (2024), where at $T_{in,EUSWH}$ of 303 and 318K, η_{EUSWH} obtained are 1.94% and 2.77% respectively.

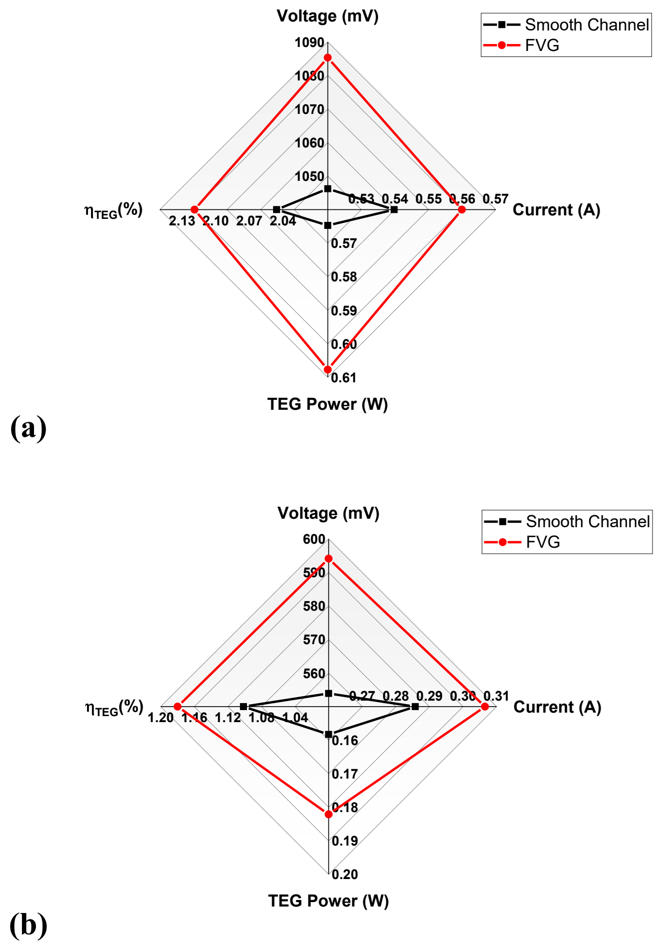

Fig. 7.13 TEG performance parameter at 313K, at (a) 0.01kg/s, and (b) 0.02kg/s

Table 7.3: Mass flow rate and inlet EUSWH temperature combination for Fig. 7.14

Channel configuration	Mass flow rate (kg/s)	$T_{in,EUSWH}$ (K)	Fig. caption
Smooth channel	0.2	313	Fig. 14 (a)
		303	Fig. 14 (b)
	0.1	313	Fig. 14 (c)
		303	Fig. 14 (d)
Channel with FVG	0.2	313	Fig. 14 (e)
		303	Fig. 14 (f)
	0.1	313	Fig. 14 (g)
		303	Fig. 14 (h)

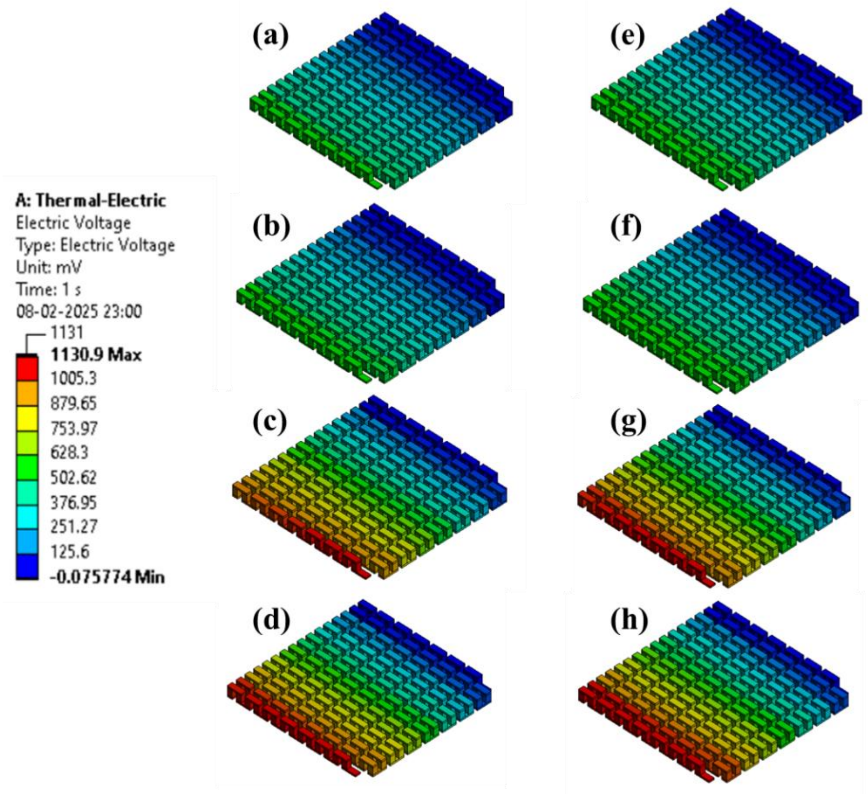

Fig. 7.14 Voltage nephograms of inner TEG for different inlet conditions as described in Table 7.3

Fig. 7.14 (a-h) shows the voltage contours of the inner TEG under different thermal and fluid flow inlet conditions. For the voltage analysis, one of the two terminals of the TEG is set as zero. This helps in the proper demonstration of the voltage distributions across the TEG. For the unambiguous Fig. notation of Fig. 7.14, the combination of inlet conditions of each contour has been described in Table 7.3. The output average voltage obtained for the smooth channel configuration (Fig. 7.14 (a-d)) with values of 553.92mV, 576.61mV, 1046.22mV, and 1091.39mV respectively. The output average voltages for channels equipped with FVGs (Fig. 7.14 (e-h)) are 594.12mV, 617.15mV, 1085.3mV, and 1130.85mV respectively.

7.2.3 Hybrid system performance

The cumulative effect of mass flow rates, $T_{in,EUSWH}$, and channel configuration on the hybrid system performance, i.e., hybrid system efficiency is shown in Fig. 7.15 (a-b). All these parameters govern the behavior of both EUSWH and TEG actions. The η_{HS} inculcates the combined efficacy of the EUSWH and TEG modules. It is defined as the ratio of TEG power output to the total incident solar radiation. Clearly, the η_{HS} is enhanced with the application of FVGs on the hot side of the TEG. The application of FVGs, results in more uniform temperature across the TEG's length. Due to vortex generators, the convective heat transfer coefficient increases, meaning heat is transferred away from the hot side more effectively. This leads to an increase in the hot side's effective temperature compared to its maximum potential, enhancing the thermoelectric efficiency. Also, at increased mass flow rates, the system may not allow sufficient time for the working fluid to heat up, lowering the temperature difference because TEGs operate optimally at a specific temperature difference. Increased flow rates also result in high heat dissipation to the surroundings. Hence the hybrid system efficiency deteriorates with increased mass flow rate. Furthermore, the temperature difference across the TEG is a critical parameter to the TEG output. As $T_{in,EUSWH}$ increases, $T_{out,EUSWH}$ also increases. But the increase in the latter is gradual and hence the TEG output decreases with increasing $T_{in,EUSWH}$. Fig. 7.15 (a) exhibits the η_{HS} at $T_{in,EUSWH}$=303K. The hybrid system efficiency increases by 7.39%, and 14.66% for 0.01 and 0.02kg/s mass flow rate, respectively, due to FVGs application. At $T_{in,EUSWH}$=313K (Fig. 7.15 (b)), η_{HS} increases by 7.62% and 15% for 0.01 and 0.02kg/s. Also, the highest and the lowest η_{HS} obtained are 0.0192% (at G=1000W/m^2, mass flow rate=0.01kg/s, and $T_{in,EUSWH}$=303K, FVG incorporated channel), and 0.0046% (at G=1000W/m^2, mass flow rate=0.02kg/s, and $T_{in, EUSWH}$=313K, smooth channel) respectively.

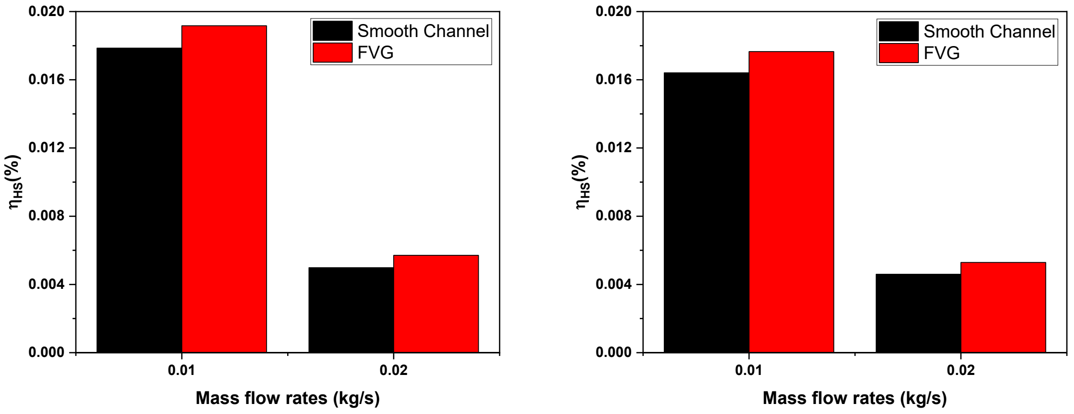

(a) **(b)**

Fig. 7.15 Hybrid system efficiency of different channel configurations at (a) 303K, and (b) 313K of $T_{in,EUSWH}$

7.3 Highlights

- It is observed that η_{EUSWH} increases with an increase in incident solar radiation, and mass flow rate, while it decreases with inlet EUSWH temperature.
- At G=1000W/m^2, η_{EUSWH} decreases by 5.55% and 4.92% at mass flow rates of 0.01 and 0.02kg/s, respectively when the $T_{in,EUSWH}$ varies from 303-313K. However, it increases by 3.88% and 4.58% at $T_{in,EUSWH}$ of 303 and 313K, respectively when mass flow rates are varied from 0.01-0.02kg/s.
- The analysis shows that the vortex generators are more efficient at lower $T_{in,EUSWH}$ and low mass flow rates.
- The application of VGs results in better TEG performance. The objective of employing VGs is clearly achieved as they result in enhanced heat transfer and uniform temperature along the channel.
- The η_{HS} is enhanced with the application of FVGs on the hot side of the TEG. The hybrid system efficiency increases by 7.39 %, and 14.66% for 0.01 and 0.02kg/s

mass flow rate, respectively, due to FVGs application at 303K. At $T_{in,EUSWH}$ =313K, η_{HS} increases by 7.62% and 15% for 0.01 and 0.02kg/s.